Nanoindentation of Gold and Gold Alloys by Molecular Dynamics Simulation

Yangzhong Li (李扬中)[1†], Anuj Goyal[1], Aleksandr Chernatynskiy[1††], Jay. S. Jayashankar[2], Michael C. Kautzky[2], Susan B. Sinnott[1†††], and Simon R. Phillpot[1]*

[1]Department of Materials Science and Engineering, University of Florida, Gainesville FL 32611

[2]Seagate Technology. 8701 Computer Ave. S, Bloomington MN 55435

† Present Address: Sino-French Institute of Nuclear Engineering and Technology, Sun Yat-sen University

†† Present Address: Department of Physics, Missouri University of Science and Technology

††† Present Address: Department of Materials Science and Engineering, Pennsylvania State University

*Corresponding Author: sphil@mse.ufl.edu

To be submitted to Materials Science and Engineering A

Abstract:

The nanoindentation hardnesses and stacking fault energies (SFE) for pure and alloyed Au are determined from classical molecular dynamics simulations. Rather than a traditional force-displacement dependence that is examined in many previous nanoindentation works, we analyze the hardness vs. force in this study, which shows features that allow us to distinguish defect nucleation processes from hardening processes. During nanoindentation, homogeneously nucleated defects interact to form V-shape lock structures, and finally form four-sided dislocations that are continuously released into the bulk, in a manner similar to the

heterogeneous Frank-Read dislocation generation mechanism. Hardness in the alloy system is predicted to be critically controlled by the ease and frequency of nucleation of new defects. Consistent with previous simulation results, the difference of the unstable and stable SFE, rather than the stable SFE along, is found to be closely related to this nucleation process, and thus to hardness.

1. Introduction

Gold is an important material due to its very high electrical conductivity and great ductility. However, consistent with this excellent ductility, gold is very soft. Traditional ways of strengthening metals include work hardening, formation of solid solutions, precipitation hardening and grain-size refinement, the underlying mechanisms of which are all associated with impeding the motion of dislocations [1, 2]. Solid solutions of gold with appropriate metallic elements (silver, copper and palladium being the most common) have increased strength and preserve the metallic bonding environment within the material. They are thus still good electrical conductors; however, the high concentration of the alloying element in traditional gold alloys (e.g., 25% in 18 karat gold) does significantly reduce the electrical conductivity via electron impurity scattering as compared to pure gold. If the solute concentration can be reduced without significantly sacrificing the strengthening ability, formation of dilute solid solutions might be an effective way of obtaining gold with good electrical and mechanical properties at the same time.

It is well-known that at low strain rates, materials are hardened by defect interactions, e.g. interactions that involve point defects (in solid solution hardening), dislocations (in work hardening), grain boundaries (in grain-size refinement hardening), and volume defects (in precipitation hardening). As stress is applied, new defects (mainly dislocations) are generated from existing dislocations and from grain boundaries (GBs). Dislocation-generated dislocations are usually produced by the Frank-Read mechanism in which pinned dislocations bow and split into two parts. GB-generated dislocations are directly emitted from the walls of a GB since the high energy of GB atoms provides a lower energy barrier for dislocation nucleation. These defect-assisted heterogeneous nucleation processes are the prevalent mechanisms in materials hardening since most materials contain defects of one kind or another. Defect nucleation from a homogeneous defect-free environment is difficult due to the large energy barrier, and the amount of energy consumed also depends on the size of the nucleated defect.

Nanoindentation (NI) is a convenient method to launch homogeneous nucleation within crystals [3-5], and gold is a good candidate to be studied by NI due to its low yield strength and high crystal symmetry. In this work, we use molecular dynamics (MD) simulation to perform NI on Au crystals with various surface orientations, and study the homogeneous defect nucleation process by making a tight connection between the indentation curve and defect structures. Many previous MD simulations of NI were performed at 0 K, and the force-displacement (F-h) deformation curve showed a smooth power-law profile in the elastic deformation region [6-11]. Simulations performed at elevated temperature (usually 300 K) introduced some thermal noise but the power-law character is still identifiable [12-14]. With the onset of plastic deformation, even at 0 K some noise is introduced to the curve as a result of the mixing of defect generation and continuous elastic/plastic hardening; analysis of the deformation curve in this region is rare [9] and of little value for defect structure analysis. In this work, we are able to eliminate much of this noise by plotting the hardness-force (H-F) curve instead of the F-h curve, and relating the defect nucleation events to the characteristic peaks on the curve, making this representation of the data more useful.

After studying the defect generation process and showing how this process leads to hardening in pure gold, we identify a homogeneous hardening mechanism involving continuous generation of small-size dislocation loops from the stress source. This resembles the heterogeneous Frank-Read mechanism which continuously generates dislocation loops of relatively large sizes. We next examine the effect of dilute solid solution alloying on defect nucleation, which has not been investigated through nanoindentation so far. The stable, γ_S, and unstable, γ_U, stacking fault energies (SFEs) and the hardness are calculated. We find that the change of hardness is more closely related to $\gamma_U - \gamma_S$, although many previous experimental works tend to relate it to γ_S [15-18].

The rest of the paper is organized as follows. Section 2 presents some background information about defects in face-centered cubic (fcc) systems, as well as the setup of nanoindentation simulations and SFE calculation on pure and alloyed gold. Section 3 presents

the analysis of the defect nucleation mechanism on pure gold. Section 4 extends this analysis to alloy systems and draw relation to the calculated SFEs. Our conclusions are in Section 5.

2. Background and simulations setup

2.1 Dislocation interactions in fcc materials

Dislocations in face-centered cubic (fcc) metals usually have a finite size in the form of partial (or extended) dislocations. When a dislocation is created in one of the closed-pack directions, e.g. [*101*], with a Burgers vector of $a_0/2$, where a_0 is the lattice parameter, it is energetically favorable for it to split into two partial dislocations [19]:

$$\frac{a_0}{2}\left[0\bar{1}1\right] \rightarrow \frac{a_0}{6}\left[\bar{1}\bar{2}1\right] + \frac{a_0}{6}\left[2\bar{1}1\right] \quad (AD \rightarrow A\alpha + \alpha D) \tag{1}$$

The reaction of Eqn. (1) occurs within the (*111*) close-pack plane defined by the red triangle ABD in Fig. 1. The energy is proportional to the square of the Burgers vector, and is favorable for this reaction by Frank's rule [20]. The region created between the two partials is a stacking fault (SF). The width of this SF depends on the (stable) SFE γ_S, with a lower γ_S resulting in a wider SF [19]. It is structurally possible that another close-packed plane shares the same [*101*] direction. This is the (111) plane defined by the blue triangle ACD in Fig. 1. A dislocation dissociation reaction similar to Eqn. (1) can also occur as:

$$\frac{a_0}{2}\left[0\bar{1}1\right] \rightarrow \frac{a_0}{6}\left[1\bar{2}1\right] + \frac{a_0}{6}\left[2\bar{1}\bar{1}\right] \quad (AD \rightarrow A\beta + \beta D) \tag{2}$$

The leading partials (αD and βD) on these two planes meet at their common [*101*] direction. Depending on the sign of their Burgers vector, the two partials can join and react to form a new dislocation [12]:

$$\frac{a_0}{6}\left[2\bar{1}1\right] + \frac{a_0}{6}\left[21\bar{1}\right] \rightarrow \frac{a_0}{3}\left[010\right] \quad (\alpha D + D\beta \rightarrow \alpha\beta) \tag{3}$$

This can happen if the two leading partials have Burgers vectors of opposite signs, i.e. the compressive stress fields of these two partials are on opposite sides of the surface ABD+ADC in Fig. 1. According to Frank's rule this reaction is favorable. The resulting dislocation produced is the Lomer-Cottrell lock (LCL), so called because its Burgers vector does not lie on any {111} planes and thus it is sessile. Accumulation of the LCL structures at different <110> directions can produce a stacking fault tetrahedron. If, instead of having opposite Burgers vectors, the two leading partials have their compressive fields on the same side, they will not react since the prospective reaction

$$\frac{a_0}{6}\left[2\bar{1}1\right]+\frac{a_0}{6}\left[\bar{2}\bar{1}1\right]\rightarrow\frac{a_0}{3}\left[\bar{2}0\bar{1}\right] \tag{4}$$

is energetically unfavorable. Thus these partials will remain mobile and respond to stress fields by gliding. When multiple partials agglomerate, as we will show in this work, they form a loop structure that can glide all together, illustrating another structural configuration alternative to LCL formation in stacking fault interactions.

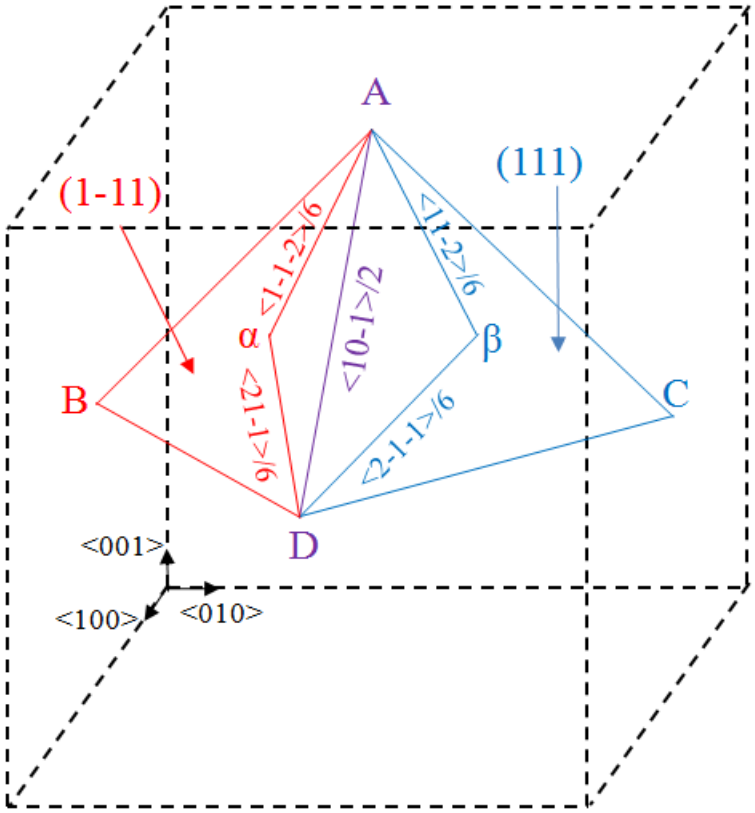

Fig. 1. Schematic of the formation of partial dislocations in an fcc system. The dotted lines form a cubic unit cell with coordinate shown at the lower-left corner. Points A, B, C and D are at the center of four faces. Triangle ABD forms the red (111) plane and ACD forms the blue (111) plane. Aα and αD are partial dislocations formed on the (111) plane by dissociating the AD dislocation. The Aβ and βD are the corresponding partials on the (111) plane.

2.2 Molecular dynamics simulation of nanoindentation

MD simulation is a useful tool to investigate defect interactions at the atomic scale. Several classical MD studies of nanoindentation in Au and other metals have been performed [6-14, 21-23]. In these work the load-displacement curves were plotted and defect analysis could be conducted. According to Hertz theory, as the system is initially under elastic deformation, the indentation force, F, increases as a power law [24]:

$$F = \frac{4}{3} E_r R^{1/2} h^{3/2} \tag{5}$$

where h is the depth of indentation, R is the radius of the indenter, E_r is the "reduced modulus" and relates the average Young's modulus and Poisson's ratio of the material (E, ν) and the indenter (E_i, ν_i) as:

$$\frac{1}{E_r} = \frac{1-\nu^2}{E} + \frac{1-\nu_i^2}{E_i} \tag{6}$$

The hardness H (sometimes referred to as "contact pressure"[25]) of the indented surface can be calculated as:

$$H = F / A \tag{7}$$

where A is the projected area of the indenter in contact with the surface. In experiment, this area is smaller than the nominal area calculated directly from the indentation depth because of the elastic sink-in deformation around the indenter. Doerner [26] and Oliver [27] have developed a method to extract the real projected area and actual hardness values from the unloading force curve. We do not implement this method here because of the relatively small indentation depth and data scatter in MD simulation can result in a large variance in the calculated hardness. Thus

A is simply defined as □= □*h*2□−*h*; small differences in the resulting hardness is expected but it would not be large enough to change the general picture and conclusion of this work.

Early MD nanoindentation works [12, 28, 29] had the shortcoming of not having a method to systematically characterize the bonding environment of atoms beneath the surface during indentation; as a result, internal atoms were masked by the surface atoms which might or might not reveal information about internal defects. This was overcome by Kelchner et al. [6] by defining the "centro-symmetry parameter" (discussed in detail below in Eqn. 9) which allowed perfectly-coordinated atoms to be distinguished from miscoordinated ("defect") atoms, thereby allowing structural defects to be identified. Rodriguez de la Fuente and coworkers [21] performed experimental and simulated indentation of the Au (100) surface. The bump-like structure seen in STM, which they dubbed a "hillock", was shown to be caused by a V-shape groove formed by two (111) SF planes in their simulation. Gannepalli and Mallapragada [12] performed NI simulation with a square pyramid indenter and showed that stress concentrated on the periphery of the indenter, leading to the formation of sessile stair-rod defect. Li et al. [30] presented a stress criterion for homogeneous nucleation and analyzed the defect structure for Al (111) nanoindentation. Lee et al. [9] investigated the defect nucleation process on Al (111) surface and observed the generation of a "dislocation embryo", which is also V-shaped. This dislocation embryo evolved into a four-sided loop that glided down to the bottom of the structure. The similarities and difference of these structures and their motions will be compared and contrasted with those seen in this work.

2.3 System setup and preparation

A gold surface structure is created in Fig. 2 with its surface normal to the z direction. The structure has dimensions of 230 Å × 230 Å × 141 Å, with an additional of 130 Å of vacuum in the z direction. The size of the vacuum must be larger than the indenter diameter so that the bottom of the structure is not affected by the presence of the indenter under periodic boundary conditions. Atoms in the bottom 5 Å are fixed in space (the grey region in Fig. 2) and support the

whole system against the downward force of the indenter. The use of this fixed portion of the surface slab to support indentation is important to predict the correct movement of defects (see text in Section 3.4). Atoms in the 10 Å thick region above the fixed region, and in the 8 Å thick region surrounding the system box side (in the x and y directions in Fig. 2) are in the thermal (black) region; they are thermostated with the Nosé-Hoover thermostat at the desired simulation temperature so that heat generated by indentation can be dissipated. All other atoms respond fully to the equations of motion and are in the so-called active region (yellow). The system size used here is similar to those used in previous works. This size is chosen so that the active region in Fig. 2 is large enough to contain all the defects generated at maximum indentation, but not so large as to prohibitively increase computational cost.

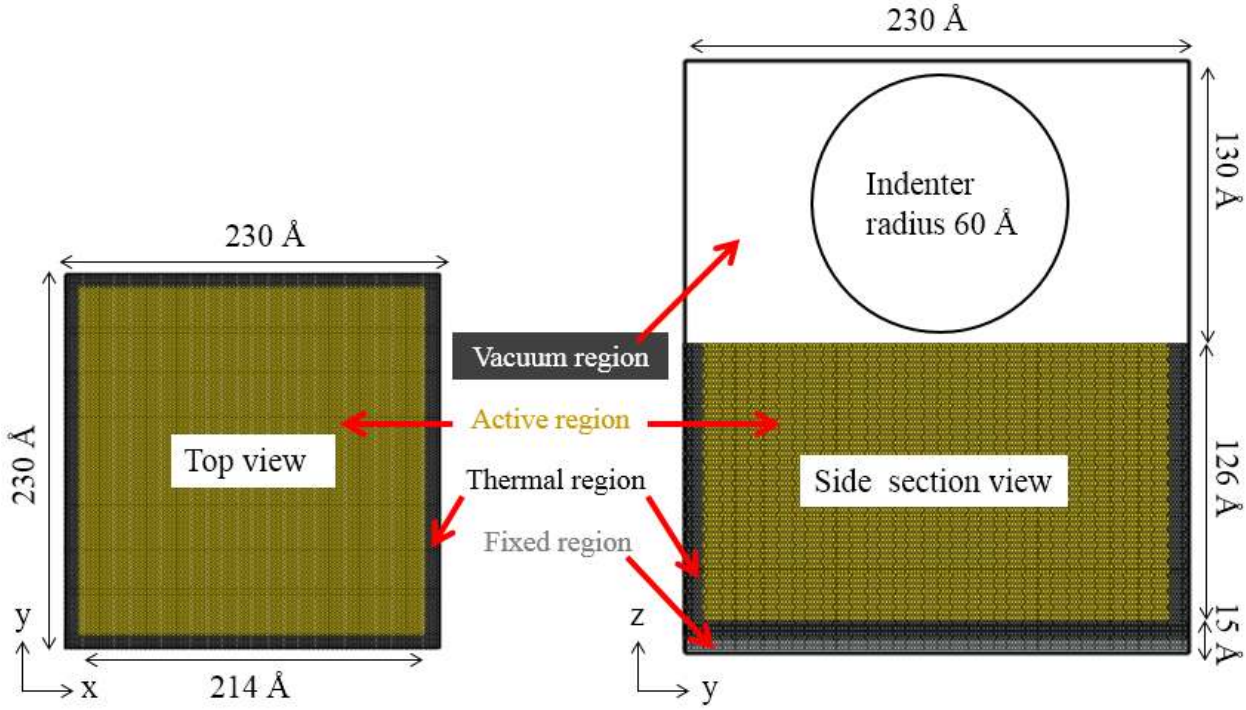

Fig. 2. Setup of the nanoindentation simulation box in this work. An indenter with 60 Å radius is pushed downward from the vacuum region with 130 Å in thickness. Atoms in the active region (yellow, 214 × 214 × 126 $Å^3$) respond by generating defect beneath the surface. The active region is surrounded by thermal region (black) of 8 Å wide in x and y direction, of 10 Å thick in z direction. A fixed region (grey) of 5 Å thick lies at the bottom to support the whole structure.

The sizes of the indenter and system are determined to yield appropriate physical behavior. As we shall see below, the structure must be indented by more than 5 Å to display any plastic deformation. However, if the ratio of the indentation depth to the indenter radius is too large, the indented surface shows "pile-up" effects [31, 32] in which atoms around the contact periphery of the indenter slide and are pushed above the original surface. Pile-up in our simulations generates a disordered state under and around the indenter, making observation and characterization of dislocations and stacking faults difficult. We find that a depth-to-radius ratio of 1:5 is an appropriate value to avoid substantial pile-up. This appears to be consistent with reports of previous Au NI simulations [6-8, 12] although this point was not discussed explicitly. Thus, under the constraints of high indentation depth and a low depth-to-radius ratio, an indenter radius of R = 60 Å and an indentation depth of z = 12 Å are reasonable choices. Due to surface relaxation, most simulations only reach a depth of 11 – 11.5 Å. All simulations are performed at T = 0.1 K. This low temperature aids the visualization of the defect structure by removing the thermal motion of atoms. The time step is 1 fs. The structure is first relaxed for 90 ps, and the indenter is applied for 120 ps in indentation mode, and another 100 ps in pull-out mode. The indenter moves at a speed of 10 m/s, which is rapid compared to experimental measurements but commensurate with MD settings [12, 32]. Slower speed of 5 and 1 m/s has been tested on (111) surfaces. The yield strength remains unchanged, but the hardness decreased by 10% as the speed reduced from 10 to 1 m/s, with similar defect structures generated. As an accurate quantitative comparison of hardness is not the primary goal in this work and slower speeds increase the computational cost proportionally, we determine that 10 m/s is a sensible choice balancing accuracy and efficiency.

The indenter-surface slab interaction is modeled as being purely repulsive. The repulsive force is described as:

$$F(r) = -A(R-r)^2 \tag{8}$$

where F is the force felt by the surface slab atoms in the direction away from the indenter center, A is the force constant that defines the bulk modulus of the indenter, R is indenter radius, r is the distance between the atom and the indenter center. Eqn. (8) only takes effect when atoms are inside the indenter, e.g. when r < R. In this work A = 10 eV/Å^3. The precise choice of A has been shown to be unimportant in a similar system and the force-displacement curve is only slightly affected [8].

The indentation simulations are performed with the EAM potential developed by Ward et al., due to its ability to handle Au and six alloying elements (fcc Ag, Al, Cu, Ni, and hcp Ti and Zr) [33]. After each simulation, the atoms are selectively plotted according to their centro-symmetry (CS) parameter, defined as [6]:

$$CS = \sum_{i=1}^{N/2} \left| \overrightarrow{R_i} + \overrightarrow{R_{i+N/2}} \right|^2 \tag{9}$$

where N is the number of nearest neighbors, Ri is the vector from the central atom to a particular neighbor *i*. For this neighbor, another neighbor *j* will be chosen so that Ri+Rj gives the smallest possible value among all neighbor atoms. Usually for high-symmetry structures such as fcc and body-centered cubic (bcc), atoms *i* and *j* are opposite neighbors of the central atom so that *j* is denoted as i+N/2. In the current simulation, N = 12 for the fcc structure. The CS parameter measures the local disorder surrounding a particular atom, and its value increases in order for atoms in perfect lattice, dislocations, stacking faults, grain boundaries and surfaces.

The hardness H is calculated as the average value of Eqn. (7) from 6 to 10 Å. Since yielding usually occurs at 4.5 – 5.5 Å of indentation, and the simulation ends after 11 Å, this average covers a reasonable range allowing different simulation conditions to be compared.

2.4 Stacking fault energy calculation

The "slab method" is used in the calculation of the stacking fault energy [34]. An fcc structure with its [*1*10], [11*2*] and [111] directions oriented to the x, y and z directions of the system is created. The structure has dimensions of $29 \times 50 \times 71$ Å^3. A vacuum layer that is 50 Å

thick is added on both sides of the z direction and periodic boundary conditions are applied to the x direction. To construct the stacking fault, the slab is divided in half along the z direction. The top half displaces along the [11*2*] direction while the bottom half is held fixed. The energy is calculated as a function of the displacement. After a complete cycle, two maxima and one minimum is obtained. The unstable SFE γ_U is defined as the smaller of the two maximums, and the stable SFE γ_S is defined as the minimum.

3. Simulations on pure Au single crystal

3.1 Preparation for result analysis

The indentation simulations of the (111), (110) and (100) Au surfaces are conducted and the curves of force vs. indentation depth (F-h) are illustrated in Fig. 3a. As mentioned in Section 1, previous simulations usually used F-h curves for result analysis, demonstrating the power-law profile in the elastic region of deformation. This profile continues until the first major drop of force appears, which corresponds to the first yielding event and the appearance of first plastic deformation. Noise in the curve appears beyond the yield point as the force is subject to competing mechanisms: a decrease in force due to defect nucleation and an increase due to indenter pressing; these effects intensify as indentation continues. Analysis becomes more difficult in this plastic region since the curve has no clear feature to characterize the defect generation process in the structure. If, instead of the force, the hardness (H) is plotted against indentation depth (H-h) [25] the curve remains roughly constant during this plastic region (Fig. 3b), albeit still with considerable oscillation. This allows a statistically meaningful value of the hardness to be extracted and error bars determined. Finally, when hardness is plotted against the force (H-F) as in Fig. 3c, the oscillations in the curve carried both in the force and in hardness largely cancel out, thereby enabling the plastic events to be more easily identified.

We now explain how the peaks in Fig. 3c form and the physical events to which they relate in the nanoindentation response. By taking derivative of Eqn. (7), we obtain

$$dH = \frac{AdF - FdA}{A^2} \tag{10}$$

So the slope of curves in the H-F plot (Fig. 3c) is

$$\frac{dH}{dF} = \frac{1}{A} - \frac{F}{A^2}\frac{dA}{dF} \tag{11}$$

As the indenter presses downward (dA > 0), the force usually increases (dF > 0). When sufficient energy has been stored, the system can relieve stress by generation of a stacking fault, accompanied by a small decrease in force (dF < 0). Each of these distinct microstructural processes takes place at a small scale and the indentation area (A) does not vary much during such a structural change. Thus, the defect generation process can be characterized by a change of slope dH/dF since the second quantity in Eqn. (11), $(F/A^2)(dA/dF)$, changes sign from positive to negative as a result of dF while the first quantity (1/A) is roughly constant throughout any given plasticity event. Such a change corresponds to an increase of slope in the H-F curve with a simultaneous decrease of F and H (because dF < 0 and dH ~ dF/A < 0), resulting in a peak pointing towards the upper right (see text in Fig. 3c). The first peak corresponds to yielding – the first defect nucleation event – and subsequent peaks correspond to further nucleation. After new defects are generated and some energy released, continued indentation causes all defects to grow in size. As a result the system undergoes a hardening process; both H and F increase again with a smaller dH/dF slope until the next defect generation process occurs.

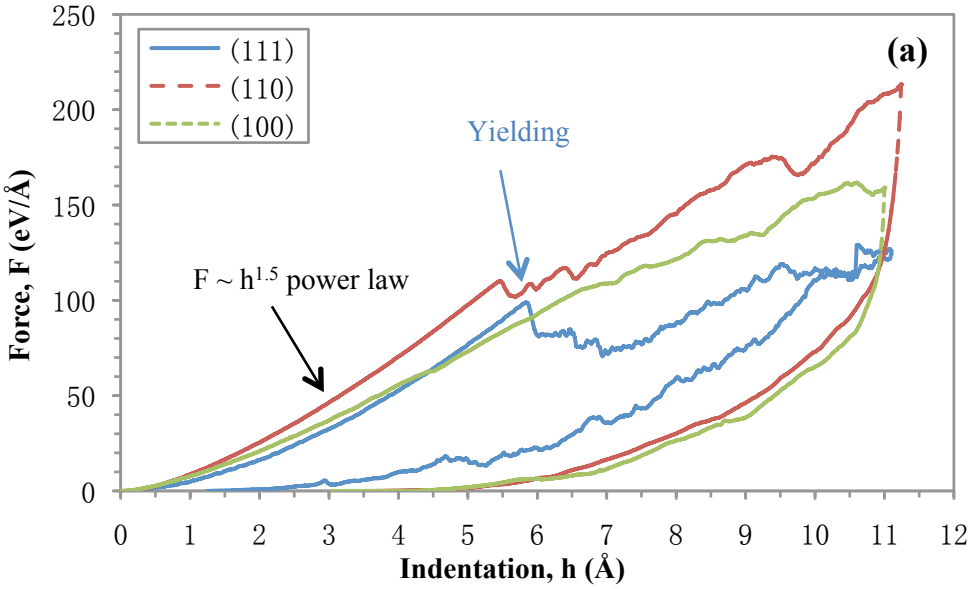
(a)
(111)
(110)
(100)
Yielding
F ~ h^1.5 power law
Force, F (eV/Å)
Indentation, h (Å)
0
50
100
150
200
250
0
1
2
3
4
5
6
7
8
9
10
11
12

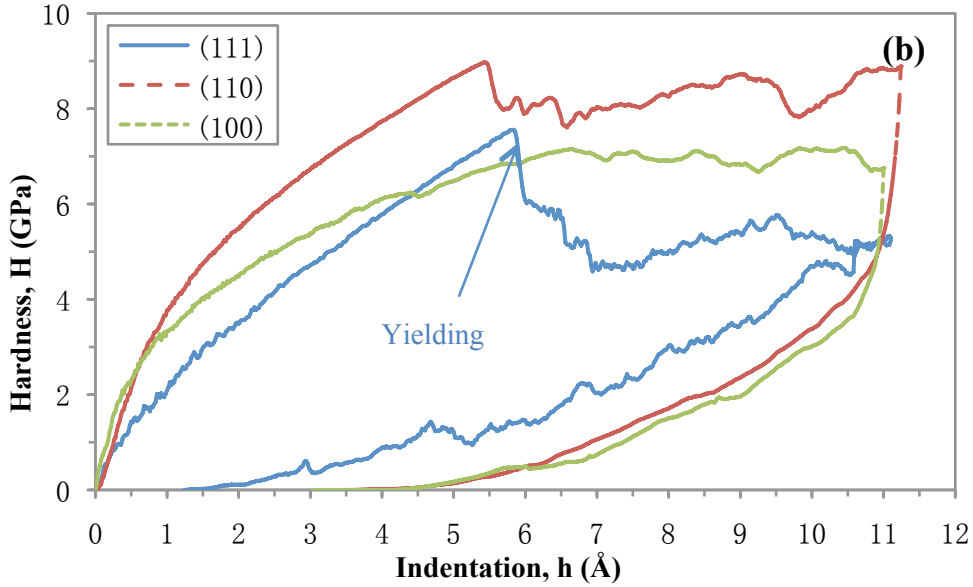
(b)
(111)
(110)
(100)
Yielding
Hardness, H (GPa)
Indentation, h (Å)
0
2
4
6
8
10
0
1
2
3
4
5
6
7
8
9
10
11
12

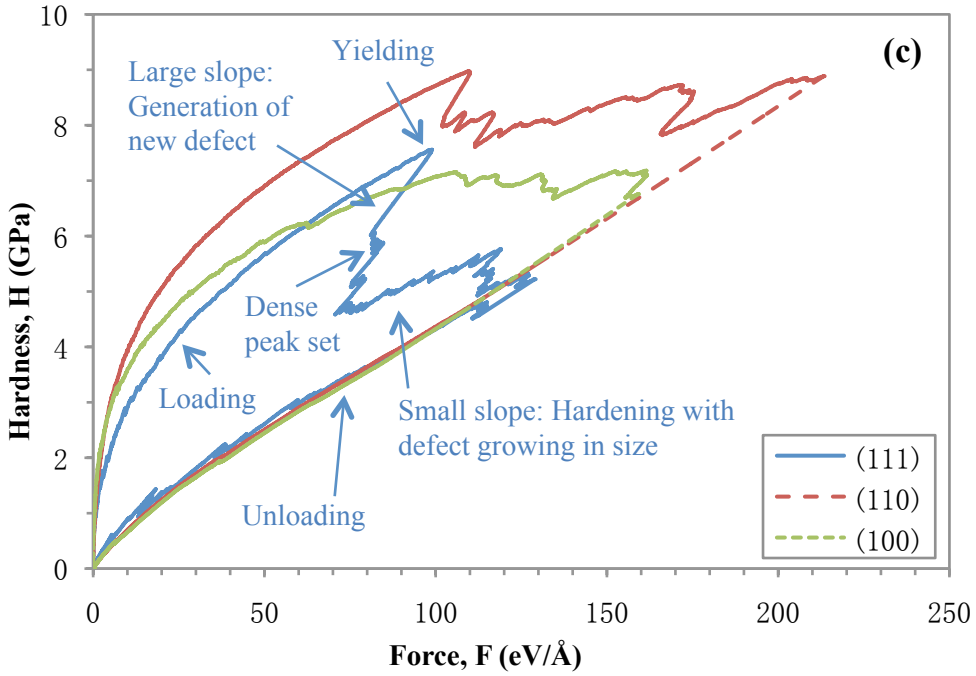

Fig. 3. Data of nanoindentation simulations on (111), (110) and (100) surfaces are shown in (a) the force-displacement (F-h) plot; (b) the hardness-displacement (H-h) plot; (c) the hardness-force (H-F) plot. The yielding points on the three plots for the (111) surface are indicated. The physical meanings of different portions of the (111) H-F curve are indicated.

The calculated yield strength of the three surfaces are compared with experimental values [35] in Fig. 4. The relative order of surface hardnesses, the (111) yield strength (7.5 GPa) and the resolved shear stress (2.0 GPa) are in good agreement with experimental values (7.3 and 1.7 GPa). Although the (110) and (100) values are a little higher, this does not affect our analysis since we are mainly concerned with the defect evolution process under the (111) surface. Nevertheless, the overall predicted physical behavior is realistic, indicating that the setup in our simulation is properly configured.

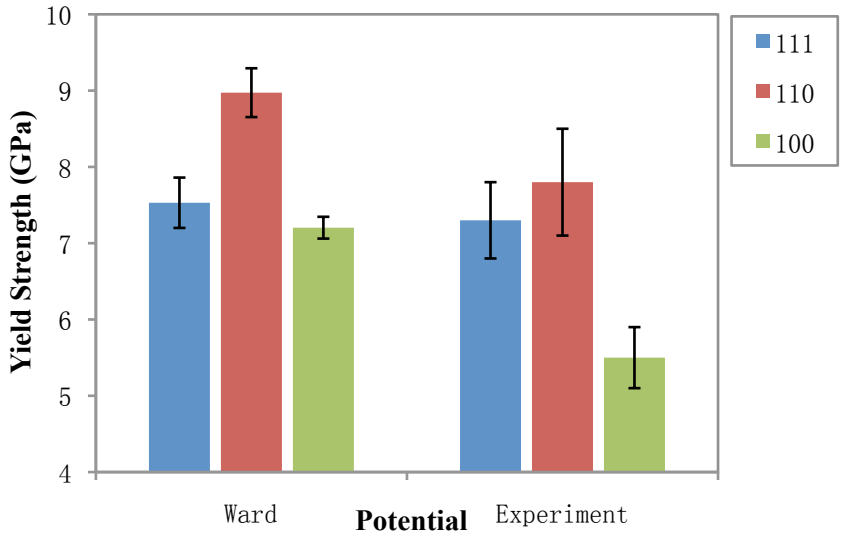

Fig. 4. Comparison of the yield strength of Au (111), (110) and (100) surfaces from EAM potentials [33] and experiment [35].

3.2 Analysis of defect generation for various surface orientations

After analyzing the representative features of an H-F curve, we can now proceed to the analysis of defect structures generated in these simulations. Fig. 5 shows snapshots of defect structures for the three surfaces at indentations of 7, 9 and 11Å. Repeated runs on the same surface produce results that are nearly identical to those shown here; so these figures can be considered representative. The defects are mainly SFs of (111) planes; however, due to the different surface orientations, the SF planes grow with a different morphology in each case. In fcc, there are four groups of {111} planes and in each group the SFs can grow in one of the three <110> directions. For the (111) system, the three plots in Fig. 3 show that the initial plastic deformation occurs at 5.6 Å, where the force (Fig. 3a) starts to drop, and continues through 7 Å indentation, triggering multiple defect generation events and reducing the hardness to 4.6 GPa. This corresponds to three groups of dense peak set in the H-F curve at F ~ 90 eV/Å (Fig. 3c), and a larger defect region for the (111) system than (110) and (100) at 7 Å indentation in Fig. 5a. Although these defects appear to be attached to the surface, they are actually nucleated homogeneously below it [6]. Stress analysis [5] showed that the position of maximum shear stress occurred below the surface, as also seen in previous MD simulations [6]. After a period of

hardening up to 9.5 Å indentation, during which existing defects grow in size and few new defect nucleates, another major nucleation event is observed and the H-F curve in Fig. 3c displays a second set of dense peaks. At this time, several large SF planes are formed. Some of them intersect and join at an angle of 70.5° (or 109.5°), forming a V-shape lock structure; this structure has also been observed in other nanoindentation works [6-9, 21, 22]. As discussed in Section 2.1, these SFs do not react to form the LCL structures (Eqn. 3) because their compressive stress fields overlap spatially. They are dubbed "locks" in the sense that once the two planes intersect, the SFs cannot continue to grow in their original directions; they can, however, either grow in their common <110> direction (along the ridge of the lock) as long as there is a stress component parallel to this direction, or grow individually at the other sides of their planes if no other plane is blocking their way. As these SF planes grow larger and consume more energy, hardening happens with both H and F increase in Fig. 3c.

The deformation process for the (110) surface is similar to that of (111) surface but with fewer nucleation events. After initial plastic deformation with relatively few peaks in the H-F curve, the system undergoes a long period of hardening that spans indentation from 6.5 to 9.5 Å. During this period, few new SFs nucleate and existing SF planes grow downward (perpendicular to the surface in <110> direction) as shown in Fig. 5e. Two sets of V-shape locks are particularly conspicuous as they form the tip of the defect structure. At 9.5 Å indentation two V-shape locks join together and release part of their structure as an individual unit, forming a prismatic loop consisting of four (111) planar regions on two different families of (111) planes (Fig. 5f). The compressive stress fields of these four SFs are all within the loop so that no LCL structure can be formed. Thus the loop is actually a full-size dislocation with both the leading and trailing partials denoted by blue atoms. The region in the interior of the loop has the same orientation as the bulk because the loop walls are intrinsic stacking faults rather than twins. This loop formation event is indicated by a large peak in the H-F curve at F ~ 170 eV/Å in Fig. 3c.

7Å 9Å 11Å

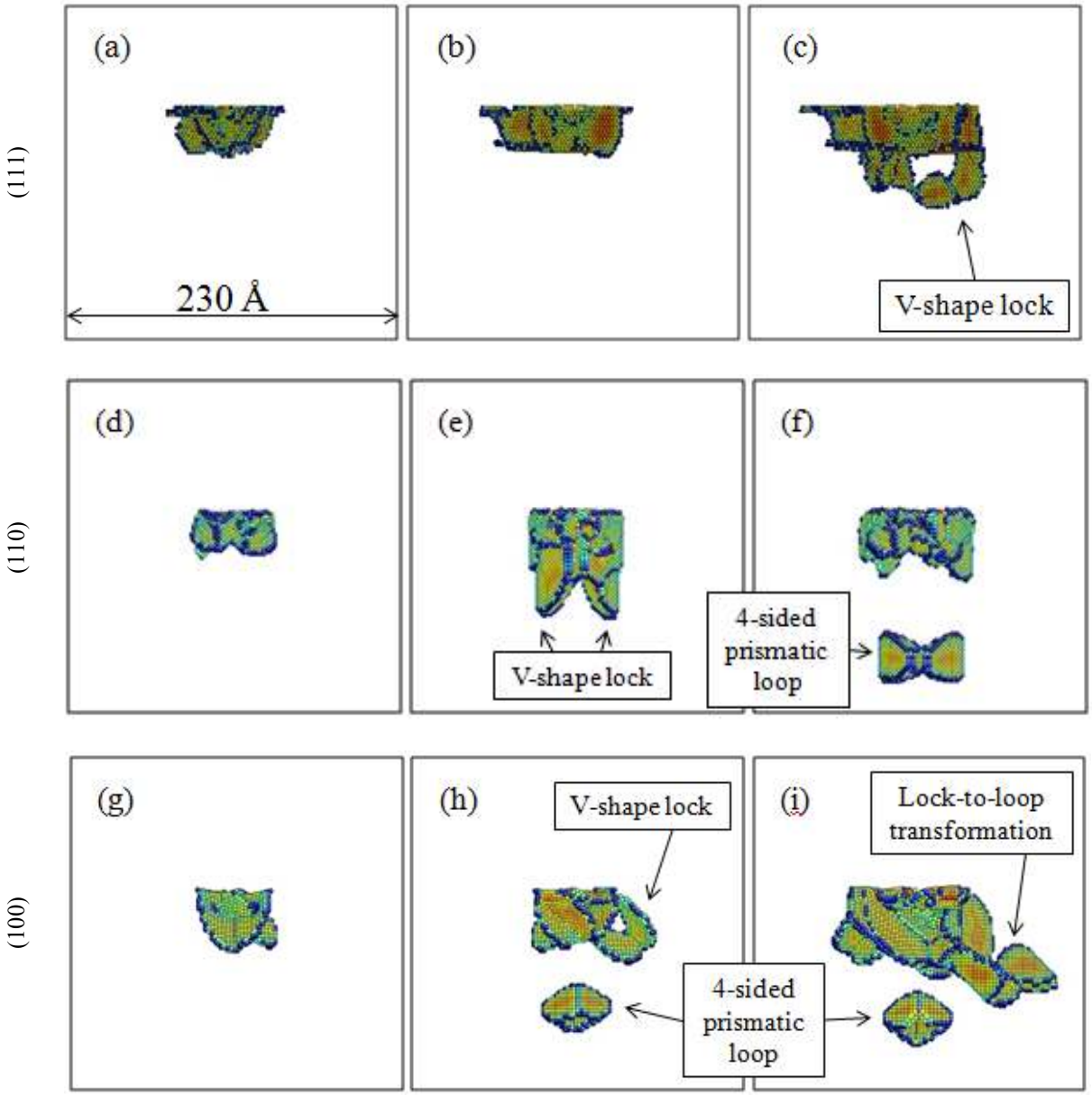

Fig. 5. Snapshots of defect structures in simulations on (111), (110) and (100) surfaces at indentation of 7, 9 and 11 Å. Indenter approaches from the top of each figure.

During the loading process the (100) system has no intense drops in force or hardness, and thus no sharp peaks in the H-F curve. The ease with which defects nucleate in this orientation is also in agreement with its low yield stress, as shown in Fig. 4. However, each shallow peak corresponds to a significant change in the defect structure. At 7 Å indentation the SF planes form a lock (Fig. 5g). A loop structure, similar to that in the (110) system, is detached

from the main defect region at 9 Å indentation, giving the third peak in the H-F curve at F ~ 130 eV/Å. At full indentation of 11Å, a second loop is forming and causing a drop of the H-F curve just before the removal of the indenter. The partial transformation of a lock to a loop can be seen in Fig. 5i.

3.3 Analysis of continuous loop generation process

To better observe the nucleation process and the movement of dislocation loops, a larger (100) system of size of 270 Å × 270 Å × 170 Å (excluding vacuum in z direction) is created. The (100) system is chosen because of its ease of generation of SFs and loops. This larger system enables an indentation 3.5 Å deeper than previous runs, anticipating that more defects will be generated. The upper portion of the hardness-force curve is shown in Fig. 6 so that more peak detail can be revealed. The corresponding indentation depths are also indicated on the curve.

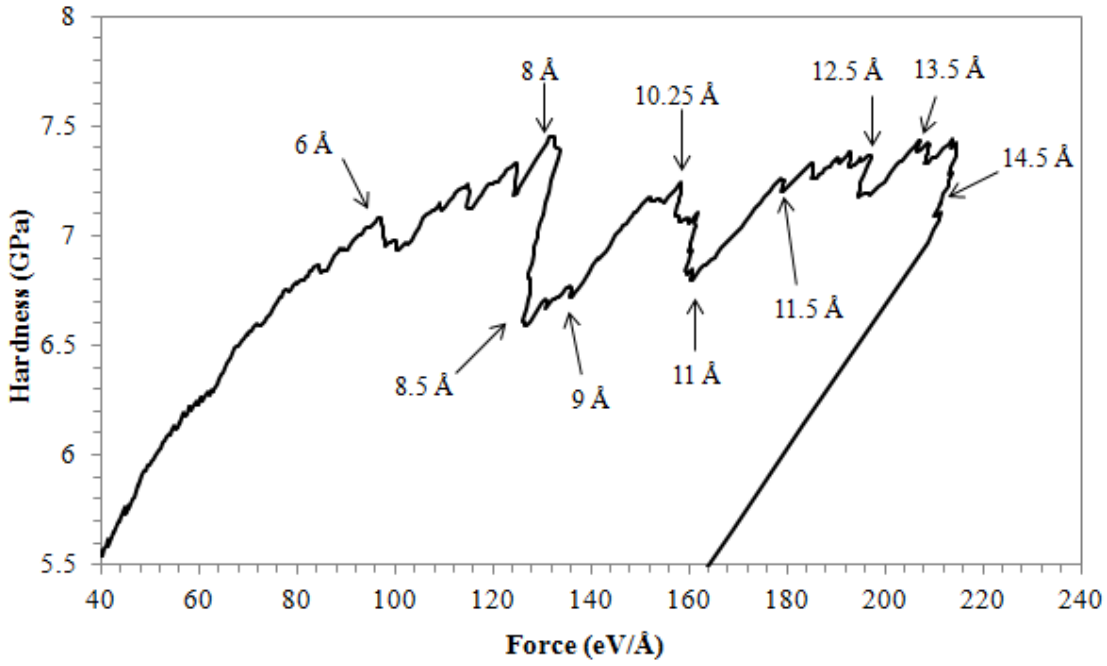

Fig. 6. Partial plot of the hardness-force curves of the (100) systems in larger sizes with dimensions of 270 Å × 270 Å × 170 Å. The depths of indentation are also indicated on the curve.

Snapshots showing the evolution of defects are presented in Fig. 7. Initial plastic deformation occurs at 6 Å indentation. After multiple SF nucleation events (multiple peaks between 6 and 8 Å in Fig. 6) at 8 Å indentation the system forms a lock structure with three stacking faults joining together (Fig. 7a). At 8.5 Å the fourth stacking fault appears and forms the prismatic loop attached to the central defect region (Fig. 7b). At 8.75Å the loop moves away from the central defect region. Three sides of the loop now disconnect from the central region, while the fourth SF starts to neck (Fig. 7c). At 9 Å the first complete prismatic loop in the system is generated and released (Fig. 7d). This event is indicated as the first major peak from 8 to 8.5 Å in the H-F curve shown in Fig. 6. The peak starts a little earlier than the actual appearance of the defect structure since the associated atomic displacement takes time to propagate from the center to the outside of the defect region. From 9 to 10.25 Å, the loop glides further away from the central region, and the system prepares for another loop release in other directions (Fig. 7e). At 11.5 Å a new V-shape lock is formed on the left side of the defect region (with a peak in the H-F curve before 11 Å), and the second loop is forming on the right side (Fig. 7f). At 12.25 Å necking occurs on the right loop at two of the connecting SFs while the prismatic loop releases, and the whole loop is finally emitted at 12.5 Å (Fig. 7g and f). From 13.25 to 13.75 Å the left SF planes start to close and form the third loop. Necking occurs at 14.25 Å and complete release occurs at a maximum indentation of 14.5 Å (Fig. 7k and l).

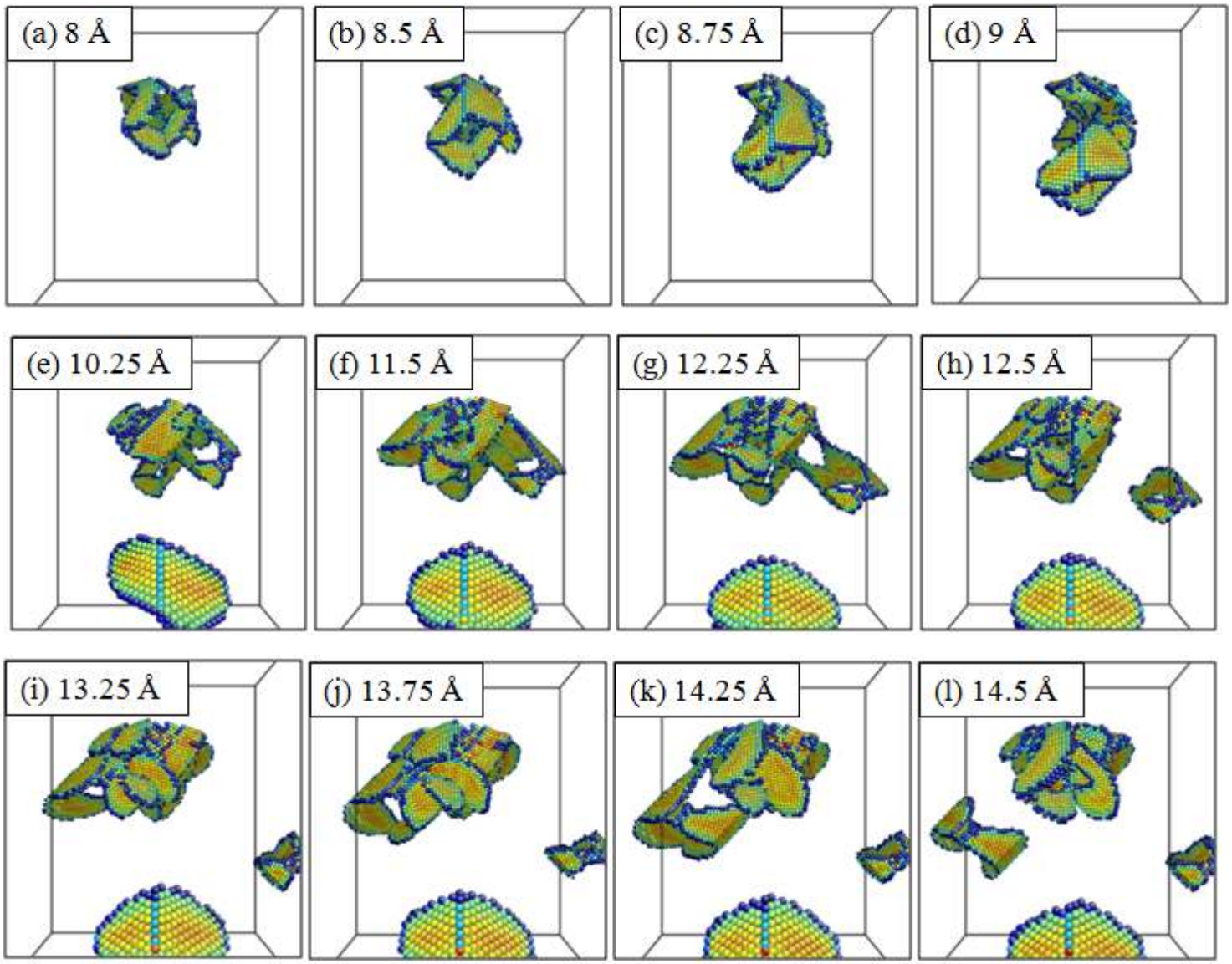
(a) 8 Å
(b) 8.5 Å
(c) 8.75 Å
(d) 9 Å
(e) 10.25 Å
(f) 11.5 Å
(g) 12.25 Å
(h) 12.5 Å
(i) 13.25 Å
(j) 13.75 Å
(k) 14.25 Å
(l) 14.5 Å

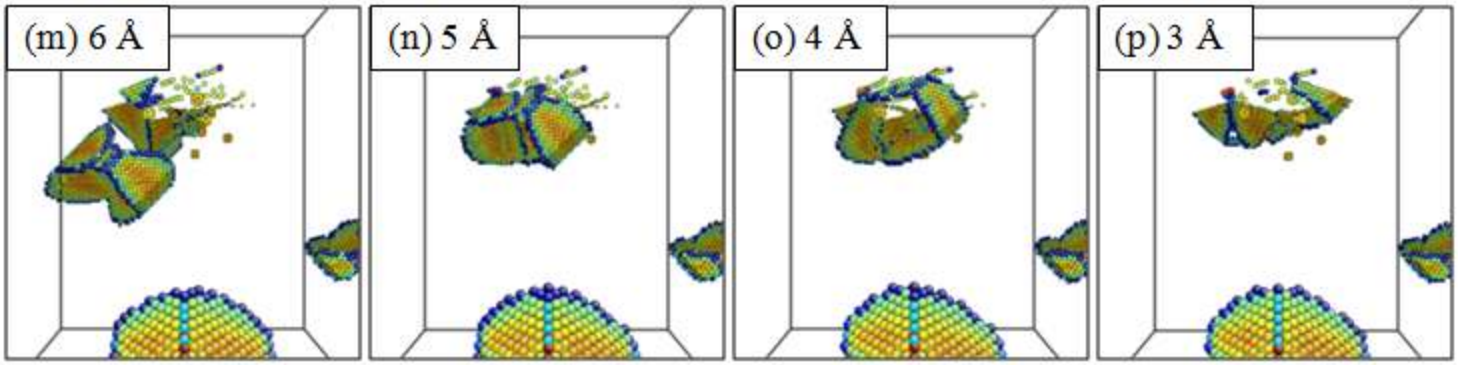

Fig. 7. Snapshots of defect structures in nanoindentation simulation on (100) surface in perspective view. The distance shown on the upper-left corner of each figure indicates the current depth of the indenter that corresponds to the depth indicated in Fig. 6. Indentation proceed from 0 Å to 14.5 Å and back to 0 Å.

As the indenter retracts, the central region diminishes and the newly-formed loop retreats slowly to its birthplace. The retreat takes place more slowly than the advance. This is because the driving force for retreat, the stress field around the loop, is much smaller than the stress field near the central region during release. As the indentation decreases from 6Å to 3Å, the loop merges with and dissolves into the surface. This contraction of dislocations is similar to the re-absorption of dislocation in 2D tensile-relaxation simulation of fcc Al [36], which indicates that newly generated dislocations are usually stabilized by external stress field. The first two loops are immobile and remain intact during the process of indenter removal, due to their large separation from their source and the minimal stress field interaction.

From the analysis above, we can now offer a clear picture of how an fcc material like Au nucleates defects homogeneously under compressive indentation stress. As plastic deformation starts, (111) stacking faults nucleate homogeneously below the surface and around the indenter. These SFs are the leading partials of a full dislocation (Eqn.1). As more SFs are formed and their sizes increase, some of them join by connecting edges of their (111) planes to form a V-shape lock structure. In contrast to the LCL structures which are also formed by SF planes, the V-shape lock remains mobile and can only grow or glide along the common <110> direction (the ridge of the "V") of its constituent planes. During this process, it may join with other SFs or locks to add more sides. Once the four sides of the lock are formed with SF planes, it is not able to absorb additional planes but can only glide or grow by increasing the length of its sides. As more and more energy is introduced into the system through indentation, the trailing partials are emitted to form a full dislocation. The trailing partial dislocations form through the necking process which repeatedly appears in Fig. 7c, g and k. Once the loop is released as a full dislocation, it is expelled by the stress field of the matrix and glides along the common <110> direction of its four sides. This prismatic loop generation process will be repeated in all possible <110> directions of the system (three possible directions in (111) system, one in (110) and four in (100)), sending dislocation loops that carry the deformation energy impulses. When the stress source is removed,

the loop may or may not retreat to its birthplace along the original path, depending on its distance from and the stress field interaction with the stress source. If the loop has been expelled too far away from the source, it will remain immobile and constitute a part of the system's permanent deformation. No loops with more than four sides are observed in this work, although loops with complicated structures could, at least in principle, form and glide, as long as all the ridges point to the same direction (which is the also the gliding direction of the whole loop) and the loop is closed so that no screw component of dislocation hinders its movement [11, 32].

3.4 Comparison with previous nanoindentation works

For materials that harden under stress, there must be one or more mechanisms that continuously operate to generate defects (usually dislocations) in order to support the ever-increasing stress. In many materials, dislocations can be nucleated heterogeneously under stress by the Frank-Read mechanism, in which dislocations are multiplied from a pinned dislocation. Dislocations and twin planes can also nucleate heterogeneously from grain boundaries as previous MD simulation works [36-39] have discussed this issue in detail. However, understanding of homogeneous nucleation, especially for nanoindentation of fcc materials, remains incomplete. Most previous simulation work discussed the process of initial nucleation [6] or V-shape lock formation [7, 8, 12, 21], but the subsequent process of lock interaction and dislocation generation has not received equal attention or analysis. Although some analysis exist [9, 11, 30, 32], no strong connections between the structure and the indentation curve have been drawn. Guided by the H-F curve, we have shown in Section 3.2 the evolution process of SFs to V-shape locks and finally to four-sided prismatic loops, as well as their roles in homogeneous hardening. As the defect structures become more complicated, their mobility decreases; stacking faults can grow or glide in three <110> directions on any {111} plane; V-shape locks can grow in only two <110> directions and glide in one common <110> direction; prismatic loops can glide in one common <110> direction and seldom grow once they detach from the main defect region. Since stress radiates from the indenter in nanoindentation, it

is very likely that all partial dislocations have their compressive stress fields on the same side facing the indenter. In other words, the formation of LCL structures (Eqn. 3) is very unlikely to happen. The V-shape locks and 4-sided prismatic loops can only be immobile when the stress direction is perpendicular to the ridge of these structures so that no stress component parallel to the ridge push them to move, a situation that is very unlikely to occur. Thus the hardening mechanism in homogeneous indentation is mainly realized by consuming energy in nucleation of SFs, lock structures and prismatic loops, in contrast to the Frank-Read mechanism in heterogeneous system. We also believe that as more prismatic loops are generated and built-up in the same direction, stress for further nucleation increases and causes strain hardening similar to Frank-Read dislocation build-up; however, direct verification would require a much larger system size and a deeper indentation depth.

Loops of similar shape to those seen here have been reported previously [9, 22, 30]; however, due to differences in the simulation conditions to counteract the indent force (these simulations applied a counter force to every atom [9] while we use a fix supporting layer, see Fig. 2), loops in these works were automatically driven under the counter force to the bottom of the simulation box and expelled. As pointed out by Yaghoobi [25], the setup of the boundary conditions and the use (or not) of the supporting fixed layer have important consequences for the evolution of defect in nanoindentation simulations. The use of a fixed layer yields almost no size-dependence of the Young's modulus (E) and H determined from simulation, and always presents the same type of defect evolution process for all system sizes [25]. By contrast, when a counter force is applied to each atom, the system shows different defect evolution modes and E and H values depending on system size. Remington et al. [11] also observed similar prismatic loop release in a bcc system; however, they did not discuss the nature of the boundary conditions used nor whether the loop glided downward automatically.

In addition to the "prismatic loop", Li et al. [30] also observed the formation of "glide loops" under the indenter. These loops were narrow and long, but did not glide as freely as the four-sided prismatic loops. Such loops have also been observed in two other nanoindentation

studies [11, 40] but not in others [6-9, 13, 14, 21]. It appears that these glide loops are essentially the same stacking faults observed in our work, but with very narrow width. The width of SFs is controlled by the γ_S of the potentials used to describe the interatomic interactions. Empirical potentials tend to have low γ_S since the SFE is not typically fitted during parameterization, so most previous simulations predicted wide SF planes and only a few predict the formation of a glide loop.

4. Alloyed Au single crystal system

From the H-F curves on pure Au system we have learned how defects evolve under indentation and how these processes correlate to the peaks on the curves. We now extend the study to alloyed systems and investigate how defect evolution processes change under alloying. Although the creation of a solid solution is one materials strengthening mechanism, our simulations indicate that low concentration alloying does not always produce strengthening. The key factor that controls strengthening will be discussed as well in this study.

The simulations are conducted in the same way as those on pure (111) Au single crystal. Random Au atoms of the original structure are substituted by alloying atoms up to the desired concentration. For each element-concentration combination, at least four simulations are conducted with different alloy atoms distribution and the average is reported. Fig. 8 shows the calculated hardness for six different elements at three different concentrations. For clarity, error bars are added for only two of these curves by showing the standard deviations of all runs for each element-concentration combination; the deviations are typically 0.1 GPa. Although we have tried hard to produce monotonic result by taking average of up to ten runs, the change of H for some elements (such as Al) at small concentration is still not large enough to distinguish themselves from the noise. Zr shows steady hardening effect from 1% to 5%, in contrast to Ti which shows steady and stronger softening effect. The other four elements have small effects on the hardness at concentration up to 5%, although we conclude that Al and Ni cause mild hardening and softening respectively at higher concentrations. These conclusions are tentative as

our work concentrates on the analysis of defect nucleation process rather than a quantitative verification of the strengthening effect.

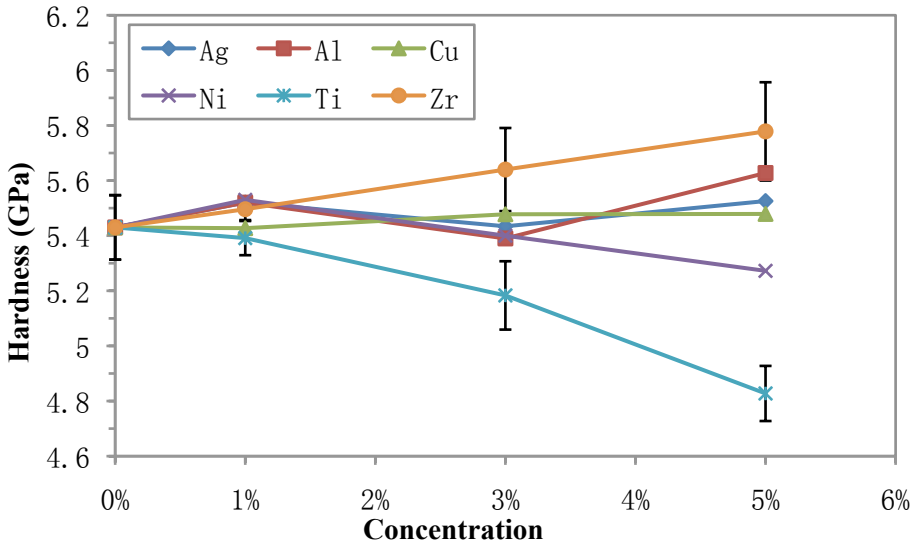

Fig. 8. Change of hardness as a function of alloy concentration up to 5% for six different elements. Error bars for Zr and Ti are added to indicate the standard deviation of all runs performed at the particular element and concentration.

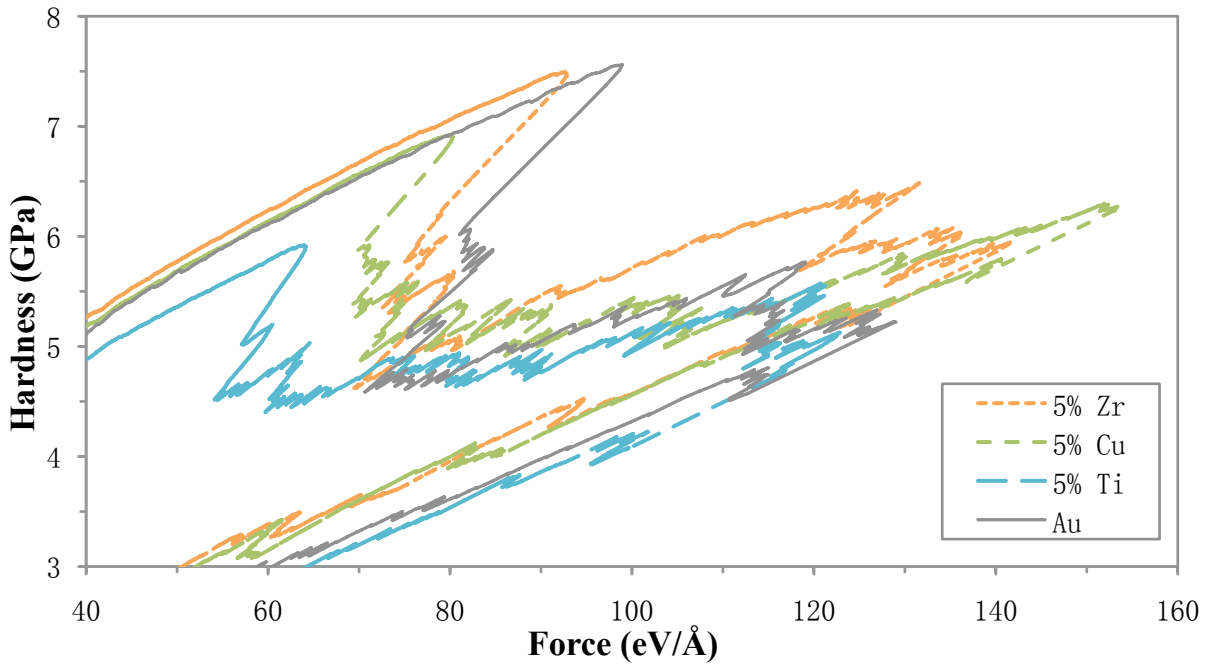

Fig. 9. The hardness-force curves of nanoindentation simulation for alloy systems with 5% Zr, Cu and Ti. The curve of pure Au is added for comparison.

In order to understand the hardening/softening mechanism and the process of defect structure nucleation, alloy systems with 5% of Zr, Cu and Ti are chosen for detailed analysis as they display the a range of strengthening/softening. Their H-F curves are shown in Fig. 9 and the snapshots of the defect structures at 7, 9 and 11 Å indentation are shown in Fig. 10. The H-F curve of pure Au is also shown in Fig. 9 for comparison. All three of these alloy systems have exactly the same distribution of alloy atoms. Analysis in Section 3.2 shows that a high hardness can also be achieved if the number of defect nucleation events is kept at minimum during plastic deformation since nucleation forms a peak in the H-F curve at which both H and F decrease simultaneously. This is what actually happens to the Zr alloy. After nucleating a few defects, this alloy system undergoes a major hardening stage from F ~ 70 to 130 eV/Å (7 – 9.5 Å indentation), during which its hardness surpasses the Cu and Ti alloys (Fig. 9). Analysis of atomic structures also shows that few defects nucleate (Fig. 10a and b) up to 9.5 Å. Nucleation of new defects after this point slightly decreases the hardness, but the average was already the highest among these three systems. The Cu alloy has a lower yield stress than the Zr alloy and undergoes major defect nucleation and interaction for indentation up to 9.5 Å (Fig. 10d and e). It then starts to harden from F ~ 100 to 150 eV/Å (9.5 – 11.5 Å) and reaches an average hardness about the same as pure Au (Fig. 9). In contrast, the Ti alloy has the lowest yield stress and most nucleation events during indentation (Fig. 10g to i). Although the system slowly hardens from F ~ 60 to 120 eV/Å (6 – 10 Å), new defects are continuously nucleating and retarding the hardening process, giving a lowest hardness.

7 Å 9 Å 11 Å

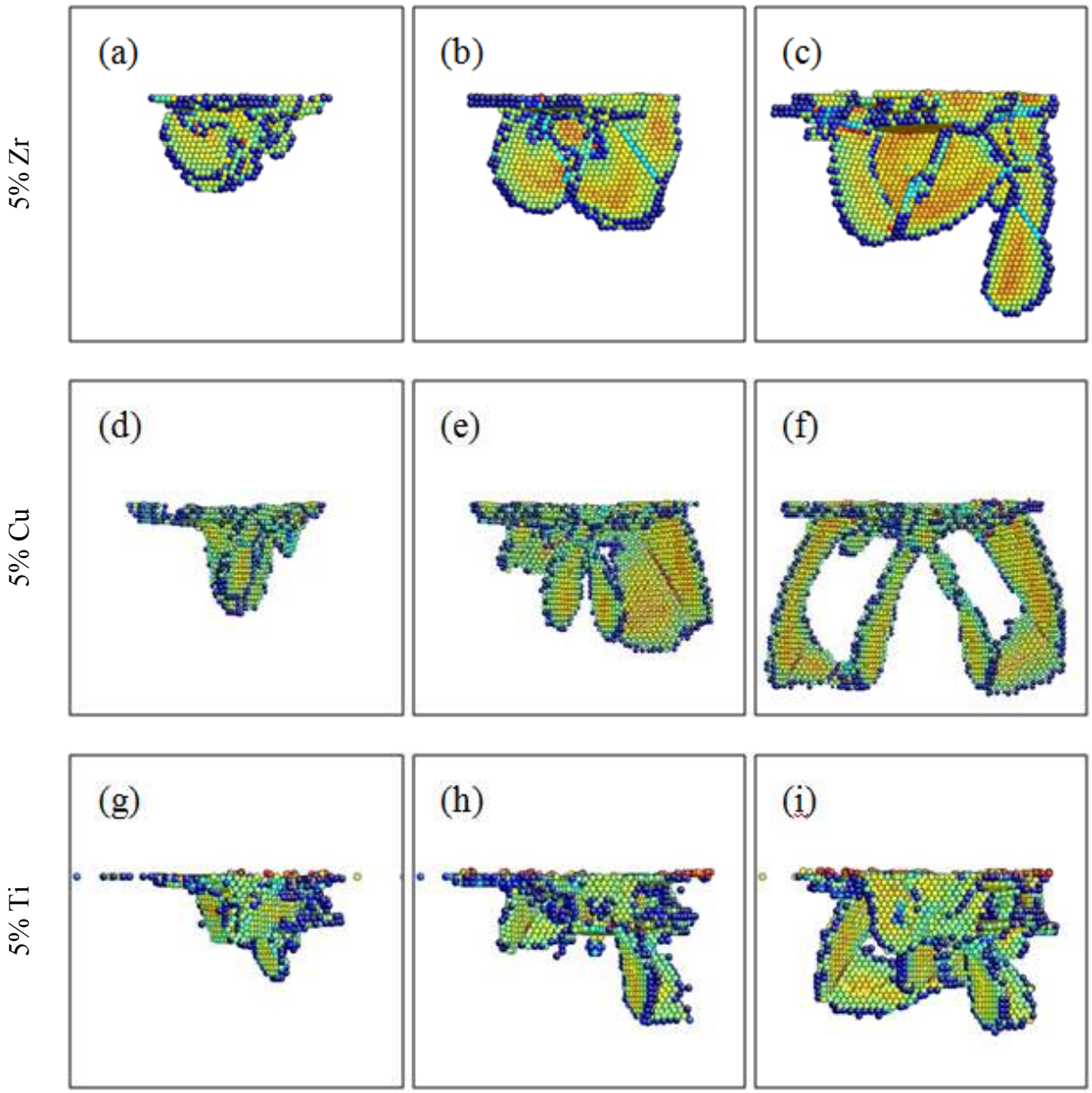

Fig. 10. Snapshots of alloy structures in nanoindentation simulations with 5% of Zr, Cu and Ti. Indenter approaches from the top of each figure. All three systems have the same alloy atom distribution.

After relating the defect nucleation process with the system's hardness, it is logical to infer that any physical quantity controlling the ease of nucleation will have a good correlation with the hardness as well. Since SFs are the most prevalent defects in our fcc pure and alloyed Au systems, we focus on the energetics of SF formation, namely, the stable (γ_S) and unstable (γ_U) SFE. Experimentally γ_S tend to decrease during alloying [16-18, 41-43] or at least remain

unchanged [44]; first principle density functional theory (DFT) calculation also showed that both γ_S and γ_U decrease during alloying of Au, if segregation to/away from the SF boundary is allowed [34]. However, this EAM potential is not specifically fit to the experimental SFE [45] of 32±5 mJ/m^2 and has a very small value of 3.6 mJ/m^2 for pure Au. During alloying, both γ_S and γ_U increase as concentration increases for most elements, except for a small decrease of γ_S in Ag and γ_U in Ti. Despite these different predictions, we still proceed with this EAM potential since it is one of the few potentials that have alloying interaction with sufficiently many elements, and the internal connection between SFE and hardness, which is the main investigation of this work, is still valid regardless of the actual SFE values.

Some experiments found that when γ_S is decreased, usually by alloying, both the yield strength and ductility increase [15-18]. Some simulation works also support this view by demonstrating the formation of full or partial dislocations in low-γ_S fcc system [36, 38], and a hardening mechanism of mutual SF blocking, twin and stair-rod lock formation [37], It has also been suggested that in addition to γ_S, γ_U should be also taken into consideration [46]. We approach this problem by MD simulation of the alloyed system in which γ_S, γ_U and hardness can be modified by adjusting the alloy concentration. By following the procedure described in Section 2.4, both SFEs and their difference ($\gamma_{U\text{-}S} = \gamma_U - \gamma_S$) are calculated as a function of concentration up to 5% for all six elements and are plotted against hardness in Fig. 11. The H-γ_U and the H-γ_{U-S} plot (Fig. 11a and c) both show high correlations and are empirically fit by a straight line do demonstrate this point. On the other hand, the H-γ_S plot in Fig. 11b shows large data scatter and no simple fit of data points is convincing. Due to a highest correlation factor, we determine that $\gamma_{U\text{-}S}$ has the strongest effect on the materials hardness for this EAM potential.

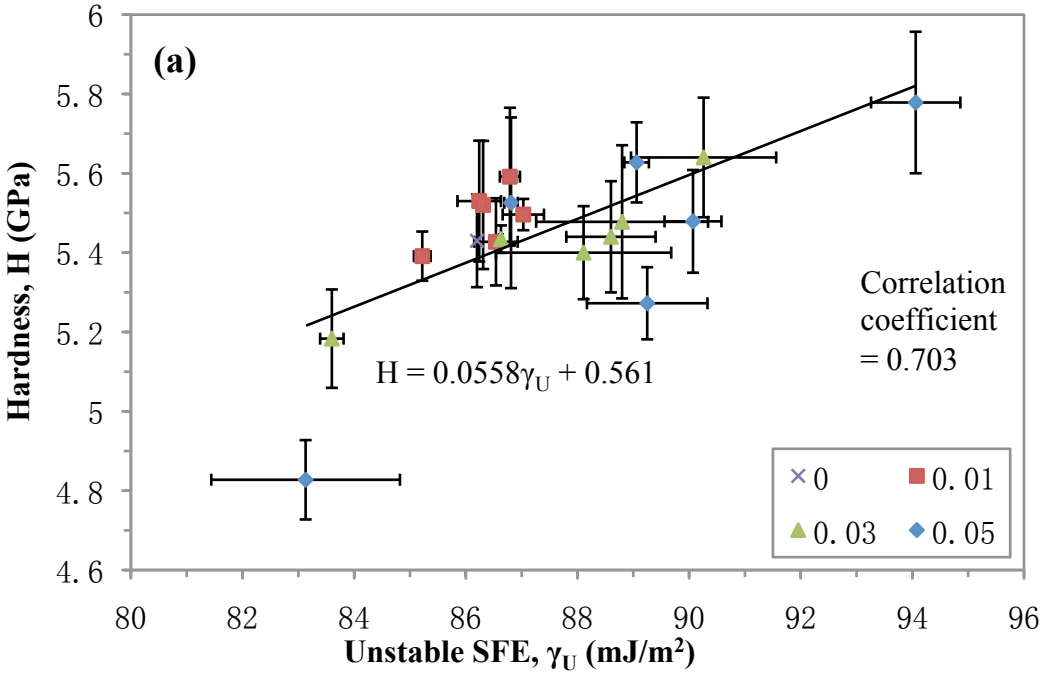
(a)
Hardness, H (GPa)
Unstable SFE, γ_U (mJ/m^2)
H = 0.0558γ_U + 0.561
Correlation coefficient = 0.703
0
0. 01
0. 03
0. 05
6
5. 8
5. 6
5. 4
5. 2
5
4. 8
4. 6
80
82
84
86
88
90
92
94
96

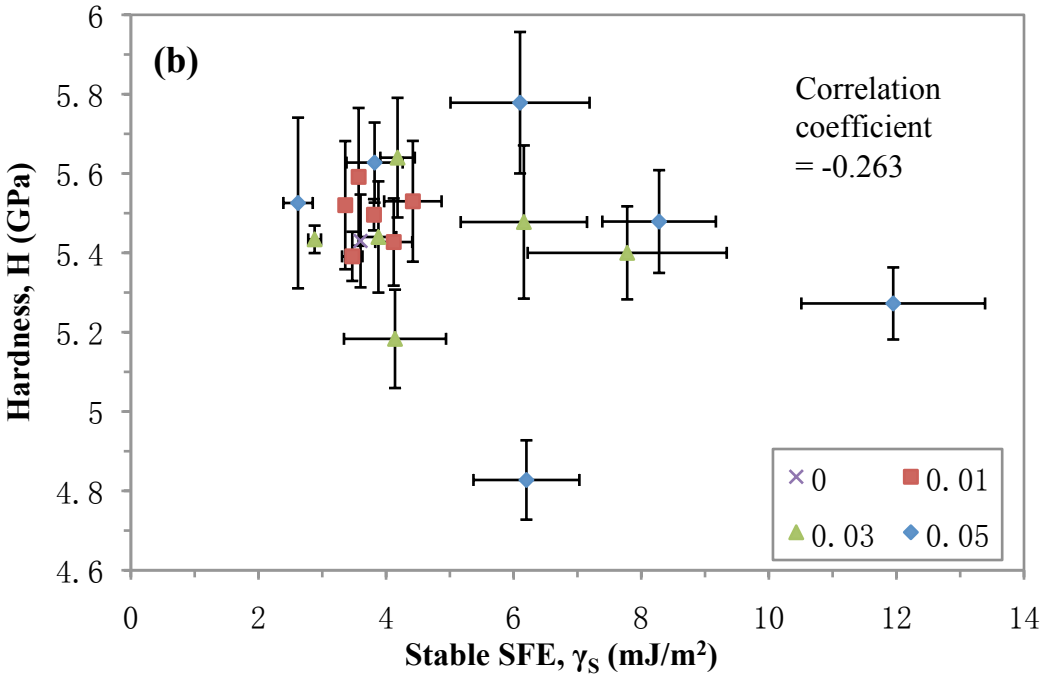
(b)
Hardness, H (GPa)
Stable SFE, γ_S (mJ/m^2)
Correlation coefficient = -0.263
0
0. 01
0. 03
0. 05
6
5. 8
5. 6
5. 4
5. 2
5
4. 8
4. 6
0
2
4
6
8
10
12
14

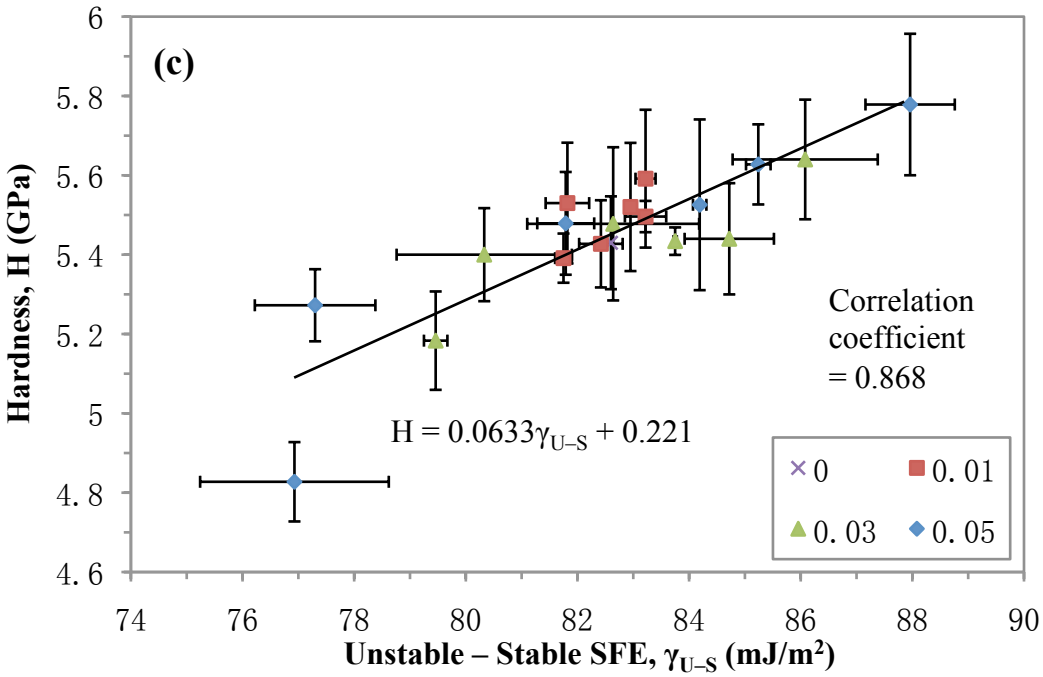

Fig. 11. The plot of hardness against (a) unstable SFE (γ_U) (b) stable SFE (γ_S) and (c) unstable minus stable SFE (γ_{U-S}) for all six alloy systems at 1%, 3% and 5% concentration. Correlation coefficient is given for all plots. A linear fit is given in the γ_U and γ_{U-S} plot to illustrate their high correlation with H. No good correlation is shown in the γ_S plot and thus no fit is given.

While forming SFs in simulation, the displaced atoms forming the leading partial need to overcome the energy barrier, whose height equals to γ_U; the atoms forming trailing partial also need to overcome a barrier of γ_{U-S}. Thus, it is expected that a material with high γ_U or γ_{U-S} values can effectively limit the activity of defect nucleation, which is shown to be helpful in increasing the hardness. The correlation between SFE and hardness (or other strength quantities, such as yield stress) has long being identified in both experiment and simulation. However, since there is no known method to measure γ_U, experimental work focused γ_S. One common and generally accepted view was that the lower the γ_S, the higher the strength of the materials. Various experimental works tried to explain this verifiable correlation. Some common explanations include that low γ_S promote formation of twinning over dislocation cross-slip [18, 42, 43] and partial dislocation over full dislocation [17, 43]. However, Fig. 11 shows a strong correlation with γ_{U-S}, but no correlation with γ_S. To reconcile the experimental and simulation results, we

conjecture that in experiment while γ_S is decreased during alloying, γ_U increases or does not decrease as much as γ_S does so that $\gamma_{U\text{-}S}$ shows an increase. An increasing $\gamma_{U\text{-}S}$ corresponds to the strengthening of the material, and experimental analyses interpret the H–γ_S correlation rather than the H–$\gamma_{U\text{-}S}$ correlation as the actual causation. DFT calculations [34] also shows that upon alloying by Ag and Cu, $\gamma_{U\text{-}S}$ of the Au alloy increases despite that both γ_U and γ_S decrease, in agreement to the well-known fact that both alloys are Au strengthening materials. Early ab-initio work found that the SFEs are dependent on the pressure [47], but we did not find pressure to be a major factor affecting γ_U or γ_S using the EAM potential. DFT calculations [34] might be more suitable to investigate the pressure dependence.

Identifying the SFE quantity ($\gamma_{U\text{-}S}$ rather than γ_S) that correlates with H has important consequences. If γ_S were the controlling factor of materials strength, there would be a theoretical limit ($\gamma_S = 0$) for strength improvement, below which the system would be structurally unstable. For example, alloying Cu with Al causes γ_S to decrease from 78 to 6 mJ/m^2 at 6% Al, while increases the yield strength by 62% [16]. If $\gamma_{U\text{–}S}$ is indeed the controlling factor, there will be essentially an unlimited range to increase γ_U.

There is one more remaining issue on the trend of SFE as concentration changes: it is not clear whether γ_S and γ_U can increase or decrease independently. From our simulation results it appears that they can, because γ_U and γ_S can both increase (as in Zr, Cu, Al and Ni) or change in opposite directions (as in Ag and Ti), making $\gamma_{U\text{–}S}$ hard to predict by just examining γ_S. However, we recall that the potential used here does not specifically fit to the experimental γ_S or the first-principle calculation of γ_U, in pure or alloyed Au. We cannot therefore conclude that these changes of SFE reflect a general trend of these alloys rather than being specific to this potential. That being said, because EAM potentials do have the capability of describing the mechanical response of metals and alloys, it is likely that this independence in trends in γ_U and γ_s is generic. Other potentials with accurate SFEs exist only for pure Au and other metals, but cross-comparison of SFE among different pure metallic systems does not help in the current analysis. DFT calculations upon alloying on seven doping elements show SFE decreases in each

case [34], but a wider range of elements has to be examined before a general conclusion can be drawn.

5. Conclusions

Using classical molecular dynamics simulation we have calculated the hardness on (111), (110) and (100) surfaces for pure gold, and on the (111) surface for gold alloyed with six elements up to 5% concentration. The stable and unstable SFEs were also calculated for these alloy systems. We introduced a plot of the hardness vs. force and showed that its characteristic peaks correspond to the defect nucleation events in the structure, enabling detailed and accurate analysis beyond the elastic deformation region to the plastic region. From this analysis we identified the detailed process by which stacking faults in homogeneous nucleation join to form V-shape locks and four-sided prismatic loops, and release into the bulk of the system as a permanent mark of plastic deformation. It was demonstrated that when Lomer-Cottrell locks are not formed, another hardening mechanism consisting of generation and movement of glissile dislocation loops is activated, in contrast to the sessile version of inter-blocking of stacking fault planes.

This analysis was extended to alloy systems and we find from the H-F curves that low-H alloys nucleate defects more frequently than high-H alloys. The barriers for nucleation - stable and unstable SFEs - are also calculated. The difference of unstable and stable SFE, corresponding to the nucleation barrier for defects, showed a strong correlation with hardness for all alloy elements at all concentration. The effect of unstable SFE and the conciliation with existing experimental results showed that an increase of the difference between unstable and stable SFE may be a more effective way of strengthening than a decrease of the stable SFE.

Acknowledgement

This work of YL, AG, AC and SRP was supported by Seagate Technology. The work of SBS was supported by Air Force Office of Scientific Research through Grant # FA9550-12-1-0456.

References

[1]J. I. Gersten and F. W. Smith, *The Physics and Chemistry of Materials*, John Wiley and Sons Inc, United States of America (2001)
[2]P. G. Shewmon, *Transformations in Metals*, McGraw-Hill, (1969)
[3]N. Gane and F. P. Bowden, Journal of Applied Physics **39**, 1432-1435 (1968)
[4]D. Tabor, Philosophical Magazine A **74**, 1207-1212 (1996)
[5]D. Tabor, *The Hardness of Metals*, Oxford University Press, New York (1951)
[6]C. L. Kelchner, S. J. Plimpton and J. C. Hamilton, Physical Review B **58**, 11085-11088 (1998)
[7]J. A. Zimmerman, C. L. Kelchner, P. A. Klein, J. C. Hamilton and S. M. Foiles, Physical Review Letters **87**, 165507 (2001)
[8]E. T. Lilleodden, J. A. Zimmerman, S. M. Foiles and W. D. Nix, Journal of the Mechanics and Physics of Solids **51**, 901-920 (2003)
[9]Y. Lee, J. Y. Park, S. Y. Kim, S. Jun and S. Im, Mechanics of Materials **37**, 1035-1048 (2005)
[10]G. Ziegenhain, H. M. Urbassek and A. Hartmaier, Journal of Applied Physics **107**, 061807- (2010)
[11]T. P. Remington, C. J. Ruestes, E. M. Bringa, B. A. Remington, C. H. Lu, B. Kad and M. A. Meyers, Acta Materialia **78**, 378-393 (2014)
[12]A. Gannepalli and S. K. Mallapragada, Physical Review B **66**, 104103 (2002)
[13]D. Feichtinger, P. M. Derlet and H. Van Swygenhoven, Physical Review B **67**, 024113 (2003)
[14]X.-L. Ma and W. Yang, Nanotechnology **14**, 1208 (2003)
[15]F. Ebrahimi, Z. Ahmed and H. Li, Applied Physics Letters **85**, 3749-3751 (2004)
[16]A. Rohatgi, K. Vecchio and G. Gray, III, Metallurgical and Materials Transactions A **32**, 135-145 (2001)
[17]Y. H. Zhao, Y. T. Zhu, X. Z. Liao, Z. Horita and T. G. Langdon, Applied Physics Letters **89**, - (2006)
[18]H. Bahmanpour, A. Kauffmann, M. S. Khoshkhoo, K. M. Youssef, S. Mula, J. Freudenberger, J. Eckert, R. O. Scattergood and C. C. Koch, Materials Science and Engineering: A **529**, 230-236 (2011)
[19]J. P. Hirth and J. Lothe, *Theory of Dislocations*, John Wiley and Sons Inc, New York (1991)
[20]J. Weertman and J. R. Weertman, *Elementary Dislocation Theory*, Oxford University Press, (1992)

[21]O. Rodríguez de la Fuente, J. A. Zimmerman, M. A. González, J. de la Figuera, J. C. Hamilton, W. W. Pai and J. M. Rojo, Physical Review Letters **88**, 036101 (2002)
[22]K. J. Kim, J. H. Yoon, M. H. Cho and H. Jang, Materials Letters **60**, 3367-3372 (2006)
[23]U. Landman, W. D. Luedtke, N. A. Burnham and R. J. Colton, Science **248**, 454-461 (1990)
[24]K. L. Johnson, *Contact Mechanics*, Cambridge University Press, Cambridge, UK (1985)
[25]M. Yaghoobi and G. Z. Voyiadjis, Computational Materials Science **95**, 626-636 (2014)
[26]M. F. Doerner and W. D. Nix, Journal of Materials Research **1**, 601-609 (1986)
[27]W. C. Oliver and G. M. Pharr, Journal of Materials Research **7**, 1564-1583 (1992)
[28]D. W. Brenner, S. B. Sinnott, J. A. Harrison and O. A. Shenderova, Nanotechnology **7**, 161 (1996)
[29]J. Belak, D. B. Boercker and I. F. Stowers, MRS Bulletin **18**, 55-60 (1993)
[30]J. Li, K. J. Van Vliet, T. Zhu, S. Yip and S. Suresh, Nature **418**, 307-310 (2002)
[31]T.-H. Fang, C.-I. Weng and J.-G. Chang, Materials Science and Engineering: A **357**, 7-12 (2003)
[32]R. Smith, D. Christopher, S. D. Kenny, A. Richter and B. Wolf, Physical Review B **67**, 245405 (2003)
[33]L. Ward, A. Agrawal, K. M. Flores and W. Windl, arXiv:1209.0619 (2012)
[34]A. Goyal, Y. Li, A. Chernatynskiy, J. S. Jayashankar, M. C. Kautzky, S. B. Sinnott and S. R. Phillpot, to be published (2015)
[35]J. D. Kiely and J. E. Houston, Physical Review B **57**, 12588-12594 (1998)
[36]V. Yamakov, D. Wolf, M. Salazar, S. R. Phillpot and H. Gleiter, Acta Materialia **49**, 2713-2722 (2001)
[37]V. Yamakov, D. Wolf, S. R. Phillpot and H. Gleiter, Acta Materialia **51**, 4135-4147 (2003)
[38]V. Yamakov, D. Wolf, S. R. Phillpot, A. K. Mukherjee and H. Gleiter, Nature Material **3**, 43-47 (2004)
[39]D. H. Kim, M. V. Manuel, F. Ebrahimi, J. S. Tulenko and S. R. Phillpot, Acta Materialia **58**, 6217-6229 (2010)
[40]H. Jang and D. Farkas, Materials Letters **61**, 868-871 (2007)
[41]Y. Zhang, N. R. Tao and K. Lu, Scripta Materialia **60**, 211-213 (2009)
[42]X. H. An, W. Z. Han, C. X. Huang, P. Zhang, G. Yang, S. D. Wu and Z. F. Zhang, Applied Physics Letters **92**, 201915 (2008)
[43]X. Y. San, X. G. Liang, L. P. Chen, Z. L. Xia and X. K. Zhu, Materials Science and Engineering: A **528**, 7867-7870 (2011)
[44]X. X. Wu, X. Y. San, X. G. Liang, Y. L. Gong and X. K. Zhu, Materials & Design **47**, 372-376 (2013)
[45]M. L. Jenkins, Philosophical Magazine **26**, 747-751 (1972)
[46]H. Van Swygenhoven, P. M. Derlet and A. G. Froseth, Nature Material **3**, 399-403 (2004)
[47]S. Ogata, J. Li and S. Yip, Science **298**, 807-811 (2002)